INL/EXT-13-30312
Revision 0

Characterization of Bond Strength of U-Mo Fuel Plates Using the Laser Shockwave Technique: Capabilities and Preliminary Results

J. A. Smith, D. L. Cottle, B. H. Rabin

September 2013

The INL is a U.S. Department of Energy National Laboratory
operated by Battelle Energy Alliance

INL/EXT-13-30312
Revision 0

Characterization of Bond Strength of U-Mo Fuel Plates Using the Laser Shockwave Technique: Capabilities and Preliminary Results

J. A. Smith, D. L. Cottle, B. H. Rabin

September 2013

Idaho National Laboratory
Idaho Falls, Idaho 83415

http://www.inl.gov

Prepared for the
U.S. Department of Energy
Office of Nuclear Energy
Under DOE Idaho Operations Office
Contract DE-AC07-05ID14517

INTENTIONALLY BLANK

ABSTRACT

This report summarizes work conducted to-date on the implementation of new laser-based capabilities for characterization of bond strength in nuclear fuel plates, and presents preliminary results obtained from fresh fuel studies on as-fabricated monolithic fuel consisting of uranium-10 wt.% molybdenum alloys clad in 6061 aluminum by hot isostatic pressing. Characterization involves application of two complementary experimental methods, laser-shock testing and laser-ultrasonic imaging, collectively referred to as the Laser Shockwave Technique (LST), that allows the integrity, physical properties and interfacial bond strength in fuel plates to be evaluated. Example characterization results are provided, including measurement of layer thicknesses, elastic properties of the constituents, and the location and nature of generated debonds (including kissing bonds). LST provides spatially localized, non-contacting measurements with minimum specimen preparation, and is ideally suited for applications involving radioactive materials, including irradiated materials. The theoretical principles and experimental approaches employed in characterizing nuclear fuel plates are described, and preliminary bond strength measurement results are discussed, with emphasis on demonstrating the capabilities and limitations of these methods. These preliminary results demonstrate the ability to distinguish bond strength variations between different fuel plates. Although additional development work is necessary to validate and qualify the test methods, these results suggest LST is viable as a method to meet fuel qualification requirements to demonstrate acceptable bonding integrity.

INTENTIONALLY BLANK

ACKNOWLEDGEMENTS

The authors would like to thank their colleagues at National Research Council of Canada at Boucherville (Daniel Levesque, Martin Lord, Christian Neron, Alain Blouin and Jean-Pierre Monchalin), as well as Mathieu Perton, for their pioneering research on this subject, and for providing support for the design, fabrication, installation and development of analysis methodologies implemented under this project. The authors are grateful for the assistance provided by Bradley Benefiel and Clark Scott in implementing these new experimental capabilities at INL.

INTENTIONALLY BLANK

CONTENTS

FIGURES

TABLES

ACRONYMS

DU	depleted uranium
FWHM	full-width at half-maximum
GTRI	Global Threat Reduction Initiative
HEL	Hugoniot Elastic Limit
HEU	highly enriched uranium
HIP	hot isostatic pressing
HMFTF	Hydro-mechanical Flow Test Facility
ID	identification
INL	Idaho National Laboratory
LANL	Los Alamos National Laboratory
LEU	low enriched uranium
LST	Laser Shockwave Technique
SS	stainless steel
STD	standard deviation
TOF	time of flight
USHPRR	U.S. High Performance Research Reactors
UT	ultrasonic
YAG	yttrium aluminum garnet
1-D	one-dimensional

INTENTIONALLY BLANK

Characterization of Bond Strength of U-Mo Fuel Plates Using the Laser Shockwave Technique: Capabilities and Preliminary Results

1. INTRODUCTION

The U.S. National Nuclear Security Agency oversees the Global Threat Reduction Initiative (GTRI), which is tasked with minimizing the use of highly enriched uranium (HEU) worldwide. A key component of that effort is the conversion of research reactors from HEU to low-enriched uranium (LEU) fuels. The U.S. High Performance Research Reactors (USHPRR) program is developing and qualifying a new high-uranium density fuel to replace the HEU dispersion fuels currently used in certain high performance reactors.[1] The new LEU fuel is based on a fuel meat made from a monolithic uranium-10 wt.% molybdenum (U–10Mo) alloy foil (typically 0.2 to 0.4 mm thick) encapsulated in 6061 aluminum cladding using a hot isostatic pressing (HIP) process, with thin (typically 25 μm) Zr diffusion barrier interlayers between the U–10Mo and cladding, as shown schematically in Figure 1.

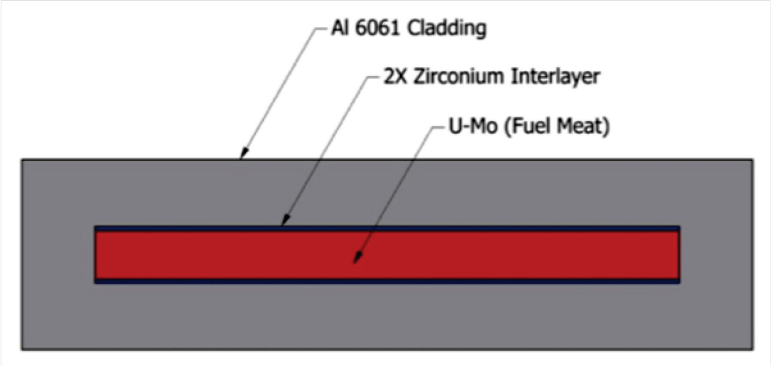

Figure 1. Schematic cross section of monolithic fuel plate.

One significant difference between monolithic fuel and historical dispersion fuels relates to the fuel-cladding interface. In monolithic fuel, a mismatch in properties exists across the fuel-cladding interface, resulting in localized stresses during fabrication and irradiation. Additionally, the interface involves complex microstructures that evolve over time. Characterizing the integrity of the fuel in both the as-fabricated (fresh) and irradiated conditions has therefore been identified as being important for demonstrating safe reactor operations and assessing fuel performance. As provided in the USHPRR Functions and Requirements document,[2] specific requirements exist to ensure mechanical stability and coolability of the fuel are maintained, and to demonstrate that fuel-cladding bonding is sufficient to prevent delamination failures. Since the cladding serves as the primary barrier for fission product retention, there are additional requirements related to ensuring that cladding-cladding bonding is maintained during anticipated operating conditions.

Measurement of bond strengths in fuel plates using conventional mechanical testing techniques is difficult. Therefore, a critical need exists to establish new evaluation methods and criteria for assessing interfacial bonding in fuel plate geometries and that can be applied to both fresh and irradiated fuels. This report describes the recent installation of new experimental capabilities at Idaho National Laboratory (INL) involving the use of laser-based characterization methods to evaluate bond strength and assess the integrity of monolithic fuel plates. The theory and limitations associated with the laser-based characterization methods are explained, along with a description of the experimental facilities and methods used in analyzing and interpreting data. Preliminary results from characterization experiments conducted on a variety of fresh fuel plate samples are presented and plans for future work are discussed.

2. BACKGROUND

The characterization techniques employed in this work to evaluate the interfacial bonding in fuel plates involves application of two complementary experimental methods - laser shock testing and laser ultrasonic (laser-UT) imaging, referred to collectively here as the Laser Shockwave Technique (LST). These techniques were originally developed for application to measurements of the adhesion of thin films and coatings to substrates.[3,4,5,6,7,8]

In these methods, a high-energy pulsed laser is used to generate a large-amplitude compression wave at the top surface of a specimen. The compressive shock wave travels through the material and after reaching the bottom of the specimen, the shock wave is reflected from the free surface as a tensile stress wave that travels back through the specimen. When of sufficient magnitude, the tensile stress generated at the film/coating interface will debond the film/coating from the substrate. By analyzing the specimen response, and with the aid of shock wave propagation models and/or dynamic simulations, the stress required to debond the film/coating from the substrate can be deduced. These techniques were later adapted for the purpose of characterizing the adhesion between layers in thicker structures such as epoxy bonded carbon-carbon composites,[9] the approach that forms the basis for the research described herein.

Advantages offered by LST include the ability to provide a spatially localized measurement without contacting the specimen, and with a minimum of specimen preparation. Since there is no propagation of the induced debond outside of the test area, the specimen remains intact. Compared to conventional testing techniques (e.g. pull testing, bend testing or double cantilever beam methods), these are significant advantages for applications involving radioactive materials. For example, nuclear fuel plates can be characterized remotely, improving operator safety, and fuel remains contained within the cladding, avoiding the potential for spreading radioactive contamination.

It should be recognized that LST is a high strain-rate interrogation technique, relying upon the propagation of waves at the speed of sound in the material. The constitutive behavior of a material under shock loading conditions is significantly different compared to that observed using quasi-static (i.e. low strain-rate) testing methods. In particular, flow stresses in metals are significantly elevated and deformation mechanisms are different at such high strain rates, therefore, the critical stress necessary to create a debond (i.e. the bond strength) as measured by LST may be several times greater than the values measured by quasi-static (i.e. low strain rate) methods such as pull testing.[10] It's worth noting that neither the high strain-rate nor quasi-static bond strength measurements can be considered to provide the "correct" answer; rather, the strengths measured are representative of the material response under the specific testing conditions used. Therefore, provided that the constituent materials and sample geometries remain fixed, and sources of error and variability in the measurements are established for the different methods, a consistent basis exists for comparison of results, and practical and meaningful correlations may be established.

3. EXPERIMENTAL TECHNIQUES

3.1 Principles and Approach

The LST experimental method relies upon a variety of hardware, software and analysis techniques that are combined into an integrated testing system. In summary, during the experiments, a high energy pulsed laser (shock laser) is fired at the top of a specimen, with incrementally increasing energy, in order to generate shockwaves with increasing magnitude within the sample. The goal is to determine the threshold necessary to create a debond at one of the internal interfaces. As will be discussed, because the shock wave energy imparted to the specimen by generation from a confined plasma is difficult to calculate or reproduce consistently, optical energy of the source laser is not an accurate predictor of internal stresses. For this reason, the system incorporates an optical interferometer whose purpose is to measure the bottom surface velocity of the specimen in real time during the shock experiments. The bottom surface velocity provides a more accurate representation of the energy actually imparted to, and transmitted through, the specimen. The recorded maximum surface velocity is therefore used in calculations to estimate the internal stresses responsible for debonding, using methods described in detail below. Finally, a pulse-echo laser-UT inspection capability integrated into the system is used to perform inspections before and after each laser shot in order to determine when a debond has occurred, as well as to measure the through-thickness location of the debond within the sample, an additional piece of information necessary to more accurately estimate the internal stress at the location where the debond actually occurred.

In general, depending upon the layer thicknesses and the dynamic elastic/plastic properties of the materials comprising the sample, the evolution of stress as a function of time at any internal location can be complex and numerous assumptions are used to interpret results. Previous publications[9,11] and the following discussion explain the strategy used to account for multiple reflections from internal interfaces, improving the accuracy and reproducibility of stress estimates.

Additional complexities are introduced into the experiments when plastic deformation occurs in the materials under the high strain rate conditions associated with shock loading. Plastic deformation changes the shape of the shock waves, dissipates energy, and further alters local stress distributions, making precise stress estimates more difficult. While evidence for localized dynamic plastic deformation has indeed been observed in the fuel plate experiments conducted to-date, as will be illustrated, the present bond strength calculations are simplified by assuming only elastic wave propagation, i.e. the effects of plasticity have been ignored. The magnitude of the error introduced into the stress estimates by ignoring plasticity has not yet been quantified, however, since we are concerned primarily with comparing results between different fuel plates comprised of the same constituents, this assumption is not expected to significantly affect the repeatability of results.

A photograph of the LST system that has been installed in the Radioactive Chemistry Lab at the INL's Materials and Fuels Complex is shown in Figure 2a, and details of the design of the optical configuration of the instrument are shown schematically in Figure 2b.

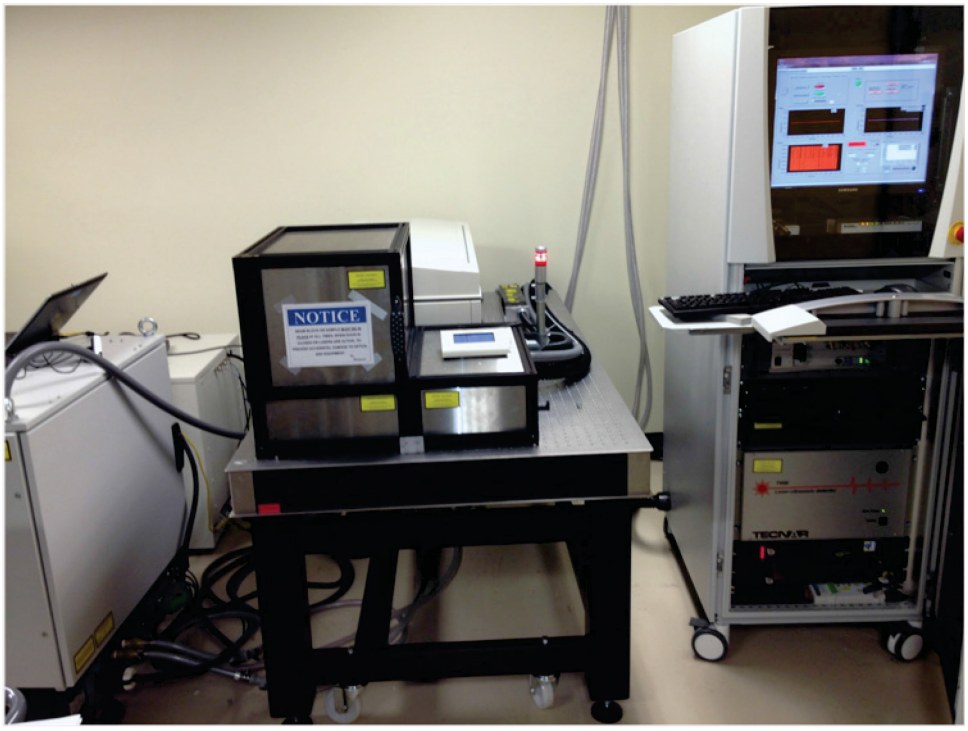

(a)

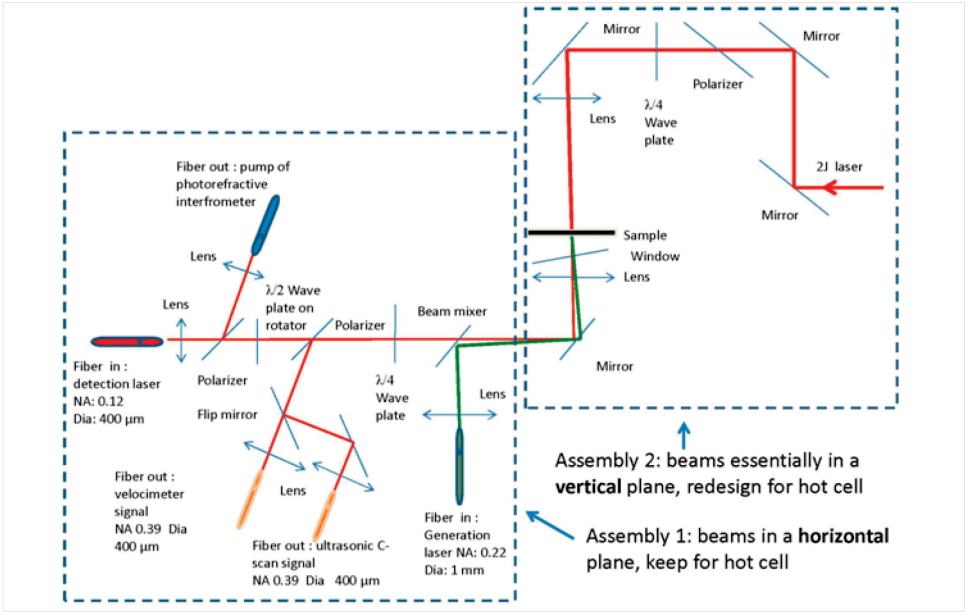

(b)

Figure 2. (a) Photograph of the INL's LST system, and (b) schematic diagram showing details of the design of the optical configuration of the system.

As show in Figure 2b, the system has been designed in modular fashion using fiber optic connections where possible. The system comprises two assemblies, labeled Assembly 1 and Assembly 2 in Figure 2b. This approach was taken to facilitate future planned implementation in the hot cell environment for the purpose of characterizing irradiated materials. Assembly 1 contains the optics associated with the laser velocimeter (described below) and laser-UT system. Assembly 1 will remain largely unchanged for hot cell implementation. Assembly 2 contains the optical components associated with delivery of the high-energy laser pulse, and the sample manipulation hardware, which will be re-designed for hot cell implementation. Plans include completing the design and fabrication activities necessary for hot cell implementation in FY14, which involves fabrication of a new feedthrough to be installed in the Hot Fuel Examination Facility at window 8M. Complete installation and in-cell equipment qualifications are currently scheduled for FY15, with the first irradiated fuel bond strength measurements to be conducted thereafter.

A Q-Switched neodymium doped: yttrium aluminum garnet (Nd:YAG) laser, which generates optical pulses of about 10 ns with a maximum energy of 3.5 J at 1064 nm wavelength, is used to induce shock waves for interrogating the top surface of fuel plates. During a shock experiment, the surface velocity of the bottom surface of the sample is recorded in real-time by an optical velocimeter based on a solid Fabry-Perot etalon. The velocimeter laser is a long pulse (>120 μs) Nd:YAG, operated at 1064 nm wavelength. Details of the etalon interferometer can be found in reference.[12] Laser-UT measurements are obtained from another sub-system, where generation and detection laser beams are applied on the bottom surface (i.e. pulse-echo mode), superimposed with diameter sizes of about 1 mm and 0.5 mm, respectively. During areal scanning, the step size of the scan is approximately 0.5 mm in the x and y directions on the sample surface. The generation laser is a Nd:YAG, operated at 532 nm wavelength with a full-width at half-maximum (FWHM) of 10 ns. The detection uses a long pulse (>120 μs) Nd:YAG laser, operated at 1064 nm wavelength and a photorefractive interferometer. The laser-ultrasonic inspection is similar to a conventional ultrasonic C-scan.

A schematic diagram showing the configuration of the sample is provided in Figure 3. In order to avoid surface damage and to increase the efficiency of optical-to-mechanical transduction, the surface of the material is covered with an absorbing tape and then covered with a transparent plasma-constraining medium (such as water or transparent tape). The shock waves generated under the confinement layer produce large-amplitude molecular displacements of the sample surface, rather than surface ablation. Previous work7,[9,13,14] used a liquid-constraining medium, e.g. de-ionized water. The liquid-constraining medium works well, but the liquid overspray can contaminate equipment and optics, and may not be desirable in the hot cell environment, therefore recent work has focused on the use of transparent tape. As stated previously, it's important to note that a simple classification of bond strength using laser power is not appropriate. In practice, there may be as much a 20% variation of laser power between consecutive shots. Also, since the properties and thickness of the confinement layer are not precisely controlled, optical absorption of the incident light may vary. Finally, the transmission of the wave through the interface between the absorptive tape and the sample depends on the bond quality, and some variability is expected. For these reasons, the velocimeter is used to record the bottom surface sample response during the shock experiments.

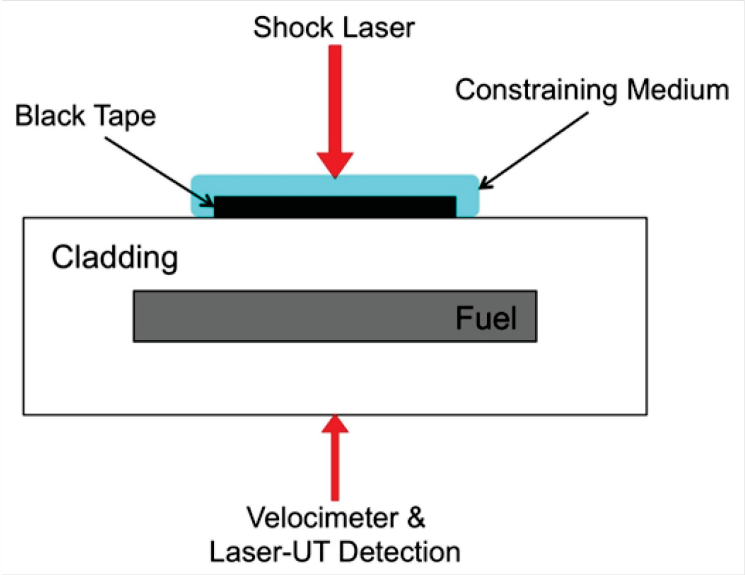

Figure 3. Schematic diagram showing the experimental configuration of a sample during analysis.

To simplify the discussions that follow, the naming conventions for referring to sample orientation and interfaces used in stress calculations are shown schematically in Figure 4. It's important to note that the identifying aspects of the fuel plate (e.g. front surface, interface I_2, back cladding, etc.) are established relative to the plate identification (ID) and are independent of the orientation of the fuel plate as measurements are being made. Alternatively, in the experimental reference frame, the laser shock is always carried out at the top of the specimen and velocimetry and laser-UT measurements are always performed from the bottom of the specimen. The Reference Orientation is considered to be the case where the plate ID is at the top, i.e. it faces the shock laser, and the Flipped Orientation is where the plate ID is at the bottom, facing the velocimeter and laser-UT detection system.

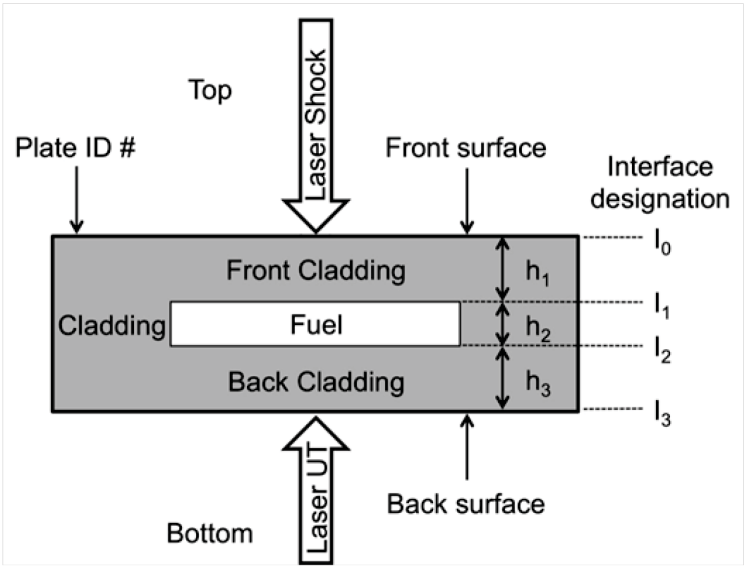

Figure 4. Geometry and sample nomenclature for a fuel plate tested the "Reference Orientation" (Plate ID at the top). Note that fuel plate characteristics are independent of the testing orientation.

In practice, the shock-wave source size (roughly equal to the shock laser spot size) is preferably chosen to be at least two times the sample thickness (about 1.5 mm for the typical fuel plates under investigation) in order to better approximate one-dimensional (1-D) wave propagation. Under the 1-D approximation, shear stresses are neglected, and the initial shock wave is primarily compressive in nature. The generated compressive shock wave travels through the specimen and is then reflected by the bottom surface of the plate as a tensile wave. It is assumed that the tensile stress waves are solely responsible for creating debonds at internal interfaces within the sample. However, stresses imposed in the material can be the result of several waves, not only the wave reflected from the bottom surface.

To illustrate this point, Figure 5 shows the time evolution of the stress amplitude in the specimen thickness imposed by an elastic wave pulse generated normal to the top surface, at time $t = 0$. This diagram was generated by an elastic numerical simulation assuming a 1-D propagation model, for thicknesses representative of the fuel plates (h_1 = 600 μm, h_2 = 280 μm, h_3 = 510 μm) and with typical wave velocity, v, and density, ρ, values as follows: for Al, v = 6.4 mm/μs, ρ = 2.7 g/cm^3, for U-Mo, v = 3.2 mm/μs, ρ = 17.2 g/cm^3.

The nomenclature corresponds to Figure 4 for a plate tested in the Reference Orientation. The temporal profile of the pulse is assumed triangular and of duration T, with a sharp compression front and a slow release (rarefaction), in close agreement with previously measured loading.9 Due to the reflections at the interfaces and surfaces, other tensile waves arise and cumulative effects results in large tensile stress concentrations at the interfaces. Note that in the geometry assumed here, the propagation times in any of the three layers are almost equal.

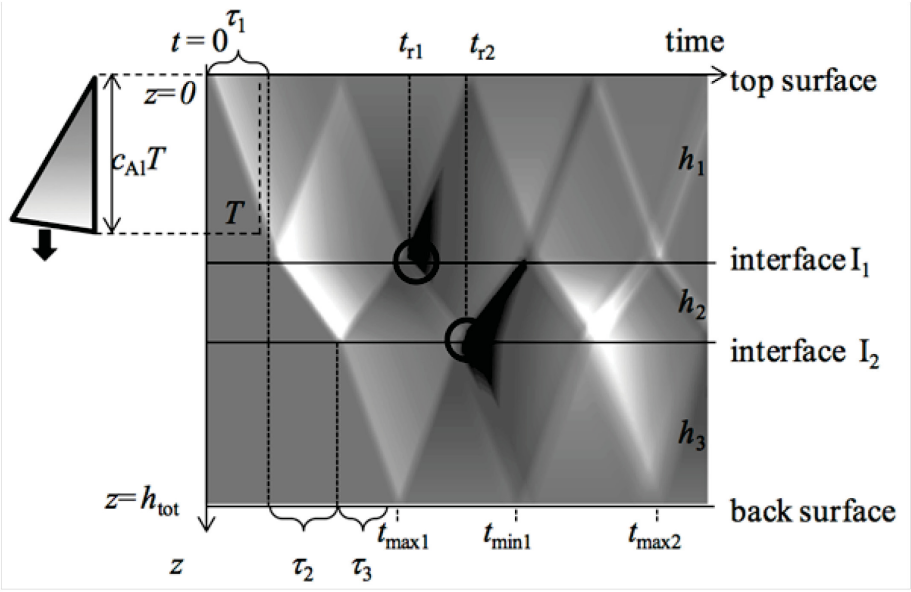

Figure 5. Time-space diagram of the propagation of a shock wave pulse. White and black areas represent the compression wave and the tensile wave, respectively.

As mentioned, bond strength is determined by increasing the laser pulse energy step-by-step and corresponds to the ultimate stress value imposed at the interface, i.e. the stress at which debonding first occurs. To minimize cumulative effects of plastic deformation in the materials, it is generally thought to be preferable to apply a single shock at each location. To evaluate the bond strength, it is assumed that debonding occurs the first time a tensile wave reaches an interface (t_{r1}, or t_{r2} in Figure 5).

The relation between the bottom surface velocity and the in-depth stress is calculated from the propagation and back propagation of the waves that reached the bottom surface up to the desired depth, while neglecting attenuation. The full derivations for obtaining the final expressions used are given in Appendix A. In these derivations, a simple, linear-elastic ray tracing method is considered for determining the stress from the measured velocimeter signal, consisting of two different sets of conditions: 1) back propagation and forward propagation (two terms), 2) including internal reflections (four terms).

The stress at the interface I_1 at time t_{r1} is calculated from the particle velocities of the four waves present at that time and that position (see Figure 5):

$$\sigma_1 = z_2 u_{01} - z_1 u_{0121} + z_2 u_{0101} - z_1 u_{012321} \tag{1}$$

where $z_i = \rho_i v_i$ is the acoustic impedance of the layer i, where u_{01}, u_{0121}, u_{0101} and u_{012321} refer to the waves that propagated from the top surface to the interface I_1, after successive reflections or transmissions denoted 0, 1, 2, 3, respectively for the top surface, the interfaces I_1, I_2 and the bottom surface. With the travel times (τ_1,τ_2,τ_3) in the different layers, the stress at the first interface becomes:

$$\sigma_1(t_{r1}) = \frac{z_3}{2T_{23}^P}\begin{pmatrix} u(t_{r1}+\tau_2+\tau_3) + R_{23}^p T_{21}^p u(t_{r1}-\tau_2+\tau_3) - R_{12}^p u(t_{r1}-2\tau_1+\tau_2+\tau_3) \\ - T_{23}^p T_{32}^p T_{21}^p u(t_{r1}-\tau_2-\tau_3) \end{pmatrix} \tag{2}$$

where $u(t)$ is the velocimeter signal at the bottom surface, and R_{ij} and T_{ij} are respectively the reflection and transmission coefficients in pressure amplitude between layers i and j. The stress value is positive for a compressive wave and negative for a tensile wave. If one considers only back propagation and forward propagation excluding internal reflections, one has Equation (2) with only the first and fourth terms. It is noticed that only the bottom surface velocity for time $t<t_{min1}$ in Figure 5 should be used in Equation (2). Also, a given indication in the bottom surface signal at time t_B attributed to the first interface is related to the stress history with the time $t_{I1}=t_B-\tau_2-\tau_3$.

The stress at the interface I_2 at time t_{r2} is calculated in the same way. Assuming no debond at the first interface, one has:

$$\sigma_2 = z_3 u_{012} - z_2 u_{01232} + z_3 u_{01012} + z_3 u_{01212} \tag{3}$$

where u_{012}, u_{01232}, u_{01012} and u_{01212} refer to the waves that propagated from the top surface to the interface I_2, after successive reflections or transmissions. The stress at the second interface becomes:

$$\sigma_2(t_{r2}) = \frac{z_3}{2}\begin{pmatrix} u(t_{r2}+\tau_3) - T_{32}^p u(t_{r2}-\tau_3) - R_{12}^p u(t_{r2}-2\tau_1+\tau_3) \\ + R_{23}^p R_{21}^p u(t_{r2}-2\tau_2+\tau_3) \end{pmatrix} \tag{4}$$

where $u(t)$ is the velocimeter signal, and R_{ij} and T_{ij} are the reflection and transmission coefficients in pressure amplitude. Again, the stress value is positive for a compressive wave and negative for a tensile wave. If one considers only back propagation and forward propagation excluding internal reflections, one has Equation (4) with only the first and second terms. Again, it is noticed that only the bottom surface velocity for time $t<t_{min1}$ should be used in Equation (4). Also, a given indication in the bottom surface signal at time t_B attributed to the second interface is related to the stress history with the time $t_{I2}=t_B-\tau_3$.

Based on the above equations, an application software under Labview™ has been developed for use with the system at INL that calculates the stress values at both interfaces of the 3-layer medium using the maximum bottom surface velocity recorded by the velocimeter during a shock experiment. It's necessary to use this software in combination with the laser-UT inspection methods to confirm that the threshold for debonding has been established and to identify which interface has debonded, and therefore which calculated stress value corresponds to the bond strength.

3.2 Materials

Samples examined in this study included experimental monolithic U-10Mo fuel mini-plates produced using fabrication processes described elsewhere,[15,16,17] as listed in Table 1. The monolithic fuel plates typically contained DU-10Mo fuel with thin Zr diffusion barrier layers clad in 6061 by a HIP process, although some plates were also examined for comparison that either contained LEU instead of DU, or did not contain the Zr diffusion barrier layer. These plates were produced as part of a previously funded HIP Parameter Optimization Study ongoing at INL, currently unpublished research, where bond strength is one of the characterizations to be performed. The "standard" HIP processing conditions involve 560 °C maximum temperature, 90 minutes hold time, 103 MPa maximum pressure, and a cooling ramp rate of 280 °C/hr. In contrast, the samples from HIP 88 involved the same conditions, except the hold time was reduced from 90 minutes to 60 minutes.[18]

Some results will also be shown that were obtained from surrogate fuel plates fabricated during the early HIP process development activities at INL, and that employed stainless steel (SS) foil as a surrogate fuel material. These samples, HIP 45-2 and HIP 46-2, were fabricated using the standard HIP conditions.

Finally, a considerable amount of work has been conducted in order to characterize a sample taken from a larger fuel plate that has been dedicated for bond strength measurement technique development. Specifically, benchmarking studies are currently underway to compare results from LST against the results obtained using other bond strength testing techniques, obtained on specimens taken from the identical fuel plate, that are currently being investigated at Los Alamos National Laboratory (LANL). The work at LANL is focused on controlled bulge testing and mini-cantilever beam testing techniques. Comparative results from these benchmark studies will be published in the future. The particular fuel plate made available for these benchmark studies was a fuel plate that was originally fabricated as part of the Hydro-mechanical Flow Test Facility (HMFTF) experiments, described in detail elsewhere.[19,20] This particular fuel plate, designated GR1286, was rejected during quality assurance inspection (for failing to meet certain dimensional requirements), but is otherwise representative of large scale monolithic fuel plates of interest to the program. The particular sample sheared from this fuel plate that was used in the present experiments is identified as OSU-1-4 in this report.

Table 1. Samples tested for which results are discussed in this report.

PLATE ID	DESCRIPTION
HIP 45-2	Mini-plate, SS fuel meat, standard HIP processing conditions
HIP 46-2	Mini-plate, SS fuel meat (known weak bond due to intentional contamination with Neo-lube)
HIP 88-2	Mini-plate, DU-10Mo fuel meat, HIP hold time 60 minutes
HIP 88-3	Mini-plate, DU-10Mo fuel meat with Zr diffusion barrier layer, HIP hold time 60 minutes
HIP 88-5	Mini-plate, LEU-10Mo fuel meat with Zr diffusion barrier layer, HIP hold time 60 minutes
OSU-1-4	Approximately 2" x 1.75" sample section from larger plate, DU-10Mo fuel meat with Zr diffusion barrier layer, standard processing conditions

4. RESULTS AND DISCUSSION

The following discussions are intended to demonstrate the functionality of the LST system, explain the experimental methodology and approaches used in data analysis, and highlight the overall capabilities of the LST methods.

4.1 Simplified Approach to Bond Strength Calculations for Preliminary Analysis of Results

Bond strength calculations accounting for multiple wave reflections (i.e. Equations 1 – 4) will be discussed later. For the purposes of an initial discussion of experimental results, the multiple wave reflections are not considered, and the measured bottom surface velocity is assumed to provide a direct first order estimate of the magnitude of the reflected stress wave responsible for creating internal interface debonds. By ignoring multiple and overlapping reflections, and assuming elastic, 1-D wave propagation and no attenuation, the measured bottom surface velocity, u_B, is related to stress at the bottom surface, σ_B, by the simplified relation given by Equation 6:

$$\sigma_B = \rho v u_B \tag{6}$$

where v is the speed of sound in 6061 Al and ρ is the density (2.7 g/cm^3).

The laser-UT inspection capabilities can be used to accurately measure v by measuring the time, t, required for a compression pulse to travel through a sample having known thickness, h according to Equation 7.

$$v = \frac{h}{t} \tag{7}$$

Note that the sample of known thickness can be, for example, a dedicated, calibrated reference standard, or a location on the actual test specimen that has been dimensionally inspected by physical means. In this manner, the speed of sound in 6061 Al, v_{Al}, has been measured experimentally to be 6,440 m/s.

By knowing v_{Al} and by measuring the total plate thickness, h_{total}, at any location, the thickness of the individual layers, namely h_1, h_2 and h_3, and the speed of sound in the fuel meat, v_{fuel}, can be determined at any specific location.

It's also worth noting the fundamental equation describing the speed of elastic wave propagation in a homogeneous, isotropic solid, assuming 1-D conditions, is given Equation 8,

$$v = \sqrt{\frac{E}{\rho}} \tag{8}$$

where E is the Young's modulus. Equation 8 allows the laser-UT characterization system to also be used in some cases to evaluate changes in material properties.

4.2 Data Acquisition and Interpretation

This section describes the real-time bottom surface velocity data that is acquired by the velocimeter during a shock experiment, and the laser-UT data generated during a post-shock scan, both of which are used to interpret the LST results.

Figure 6 shows the typical bottom surface velocity signals from measurements made on a fuel plate for three laser energies, starting from a value well below the debonding threshold, and increasing to values just above the debond threshold for interfaces I_1 and I_2. While laser energy should not be considered a measure of bond strength, the velocity signals do provide an indication of the material response.

The first acoustic pulse, located between 300 and 450 μs corresponds to the generated wave that travels through the entire sample and arrived at time t_{max1} in Figure 5. A small step at about 10 m/s, denoted HEL_1, corresponds to the aluminum Hugoniot Elastic Limit (HEL), i.e. the threshold between elastic and plastic behaviour in aluminum at high strain rate. Another step at about 25 m/s, denoted HEL_2, is presumed to correspond to the HEL of the fuel. The front of the shock waves below HEL_1 are similar for all laser energies and correspond to the so-called "precursor wave", which propagates at the elastic velocity. Behind these front waves follow a larger amplitude signal that evolves differently depending on laser energy. This corresponds to the so-called "plastic wave" which is associated to the plastic deformation. The wave propagation is therefore clearly in the "elastic-plastic regime".[21,22,23] Although not a current focus in this work, the results from the deformed temporal shape of the pulse could provide information about the high strain rate elastic and non-elastic material properties, such as yielding, strain hardening, visco-plastic flow, etc.[21] It's also worth noting that other, smaller non-linear effects come from the generation mechanism itself, i.e. the ablation in a constrained medium, or from the shock propagation where the wave propagation velocity is dependent on the local pressure. These velocity signals were all recorded for the same plate thickness, so the non-linear effects observed in the pulse shapes are easy to visualize. Nevertheless, it's important to recognize that non-linearities occur during propagation, so the shape of a pulse observed at the bottom surface can be different from the shape at a different (e.g. internal) location. These effects are not considered in the present analyses.

For the signal obtained at 400 mJ laser energy, the compression pulse (positive velocity signal) is then followed by a tensile pulse (negative velocity signal between 450 and 650μs) which corresponds to the sum of three waves, each undergoing two reflections inside any one of the three plates (arrivals around t_{min1} in Figure 5). When the signals are normalized, Figure 6b, distinct signatures (indicated by arrows) are observed for the two velocity signals obtained at larger laser energies. These are attributed to interfacial debonds that change the local reflection conditions.

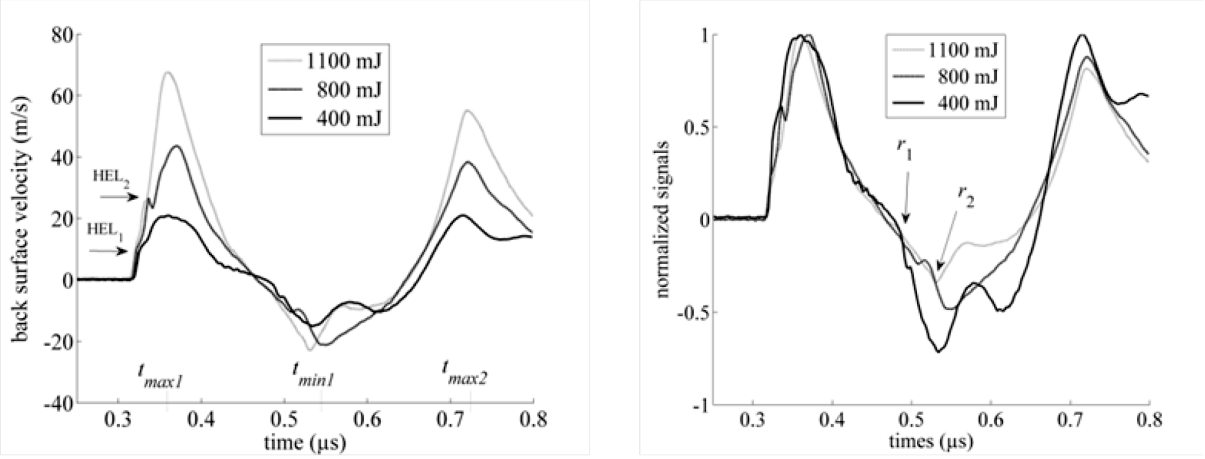

(a) (b)

Figure 6. (a) Example bottom surface velocity signals measured for laser shock pulse energies below any interface debond (400 mJ), at interface I_1 (800 mJ) and I_2 (1100 mJ) debond thresholds. (b) Same signals normalized.

Figure 7 provides an example of laser-UT characterization performed on an area of fuel plate HIP 46-2 that was known from prior UT inspection to contain a laser shock-induced debond. This figure illustrates the post-shock signals acquired and processing used to characterize the sample. Figure 7a is a convention ultrasonic C-scan image of the sample taken after the laser shock experiment, in which several debond indications are present. The laser-UT scan was performed on the area indicated, with two large debonds clearly evident. Figure 7b and 7c show the results of the laser-UT signals obtained from the scan at well-bonded and debonded locations, respectively. In Figure 7b, the cursor was placed at a nearby well-bonded location, marked position A. In Figure 7c the cursor was placed directly over the debond at position B. In Figure 7c, by directly comparing the raw and filtered A-scan data (amplitude vs. time) from the two different cursor locations, the presence of the debond is clearly evident (note the signal inversion in the A-scan at about 0.23 and 0.48 μs). The two large debonds are readily visible in the laser-UT C-scan images, which are generated by mathematically correlating the filtered raw data from the two different locations. The B-scan data, which represents the time history of amplitude along a line (in this case along the x-axis), clearly shows the presence of the original interfaces in Figure 7b and the multiple, new longitudinal and shear wave reflections created by the presence of the debond in Figure 7c. Note, the depth of the debond (i.e. the determination of which interface is debonded, I_1 or I_2) is calculated from the A-scan data by knowing the arrival time and the speed of sound in the material.

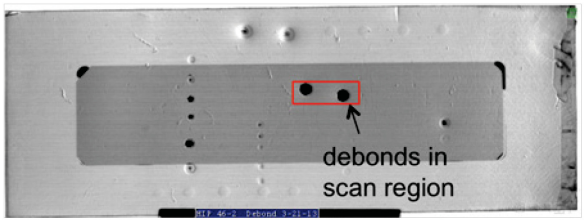

(a)

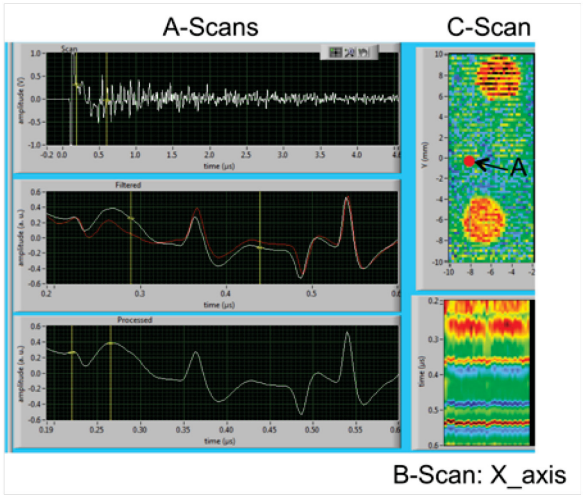

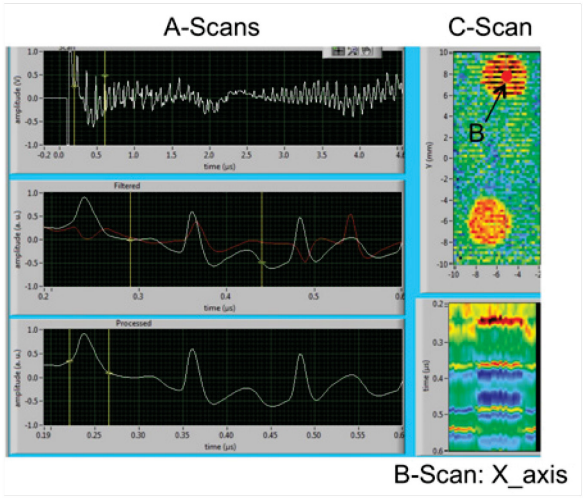

(b) (c)

Figure 7. (a) Conventional ultrasonic C-scan image of laser shocked fuel plate HIP 46-2 showing debonds in example laser-UT scan area. Laser-UT scan with signals shown for cursor positioned at (b) well-bonded spot, and (c) debonded spot.

4.3 Laser-UT Debond Characterization

The following examples are intended to demonstrate the evaluation methods used to assess debonds that are created by the laser shock when the debond threshold has been exceeded, as evidenced by the appearance of debonds in laser-UT C-scans.

An example of a shocked fuel plate exhibiting a debond at the front interface (interface I_1) that was inspected in the Reference Orientation is shown in Figure 8. Note the peak marked C in the red curve, which was taken from a well bonded region, and that represents the wave that traveled from the bottom of the plate to the top surface (front surface in this case) where it was reflected and traveled back. In the white curve, taken with the cursor positioned over the debond as shown, this particular reflection is absent, and instead, peaks marked A and B appear. Peak A represents the wave that traveled from the bottom of the plate to the debond, where it was reflected and traveled back. Peak B represents the wave that is reflected once between interfaces I_1 and I_2 (i.e. reverberated within the fuel layer itself) and then travels back to the bottom surface.

An example of the same shocked fuel plate (shown in Figure 8) that was inspected in the Flipped Orientation is shown in Figure 9. Note, for the signal in red that was taken from a well bonded region, the peaks marked B and C correspond to reflections from interface I_1 and the top surface (the back surface of the plate in this case), respectively. Now, in the signal taken from the debond region, the signal does not pass interface I_1 and only the multiple reflections between I_1 and the bottom surface are observed.

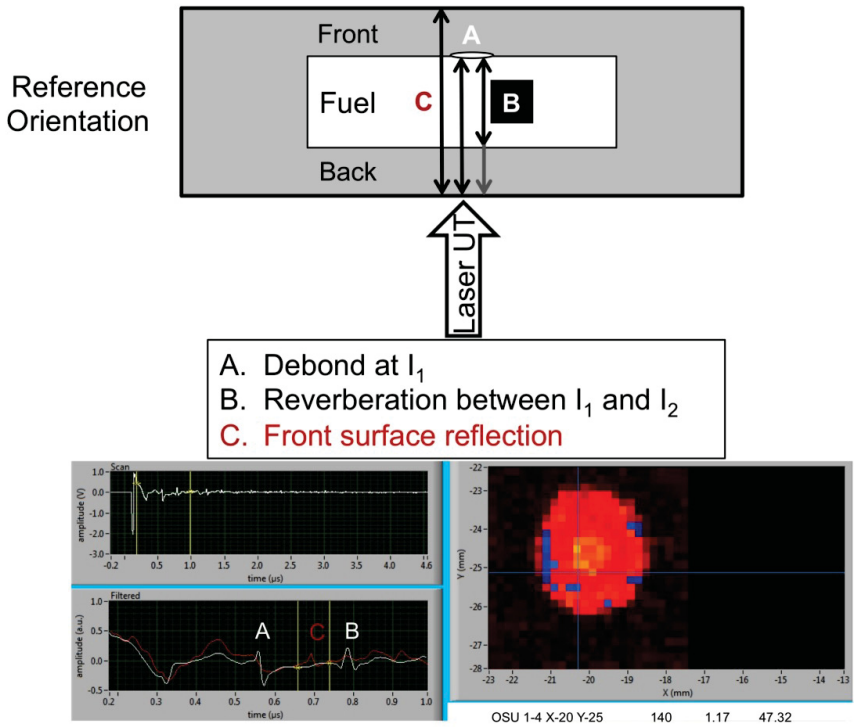

Figure 8. Example of shocked fuel plate containing a debond at interface I_1 inspected in Reference Orientation.

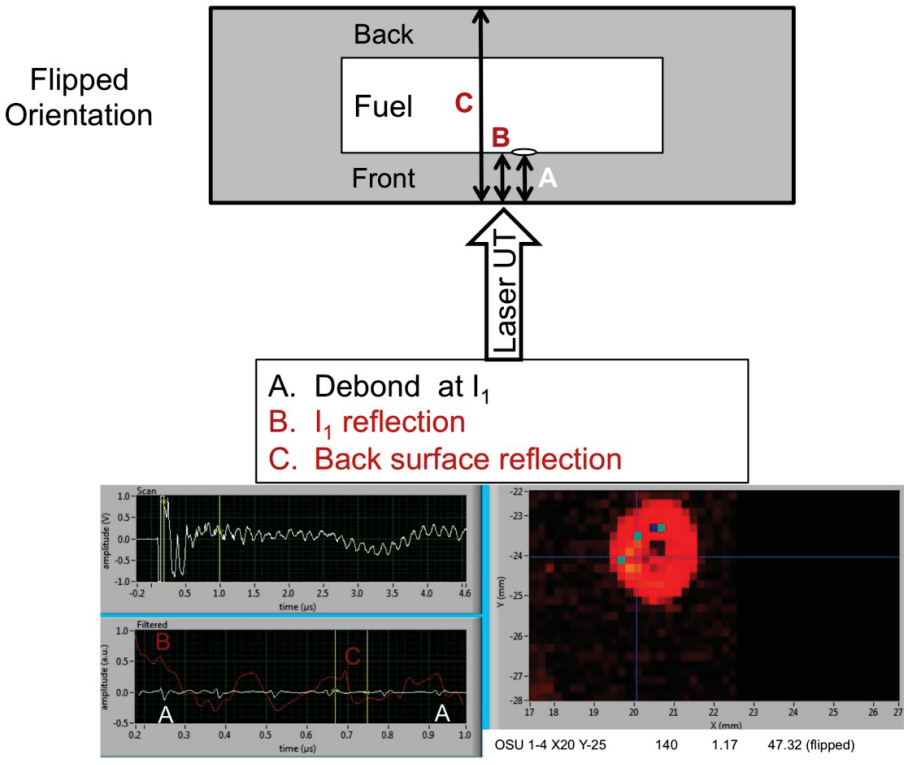

Figure 9. Example of shocked fuel plate containing a debond at interface I_1 inspected in Flipped Orientation.

In some cases, it has been observed that a single laser shock wave can actually result in debonds occurring at both interfaces I_1 and I_2. An example of this type of behavior, for a fuel plate tested in the Reference Orientation, is shown in Figure 10. Notice the signals taken from slightly different locations, both over the apparent debond region in the C-scan, are significantly different. The signal for the location shown in the upper image is indicative of a debond that exists at interface I_1 (similar to Figure 8), while the signal for the cursor location shown in the lower image is indicative of a debond at interface I_2 (similar to Figure 9). Therefore, clear evidence is present that both interfaces are broken.

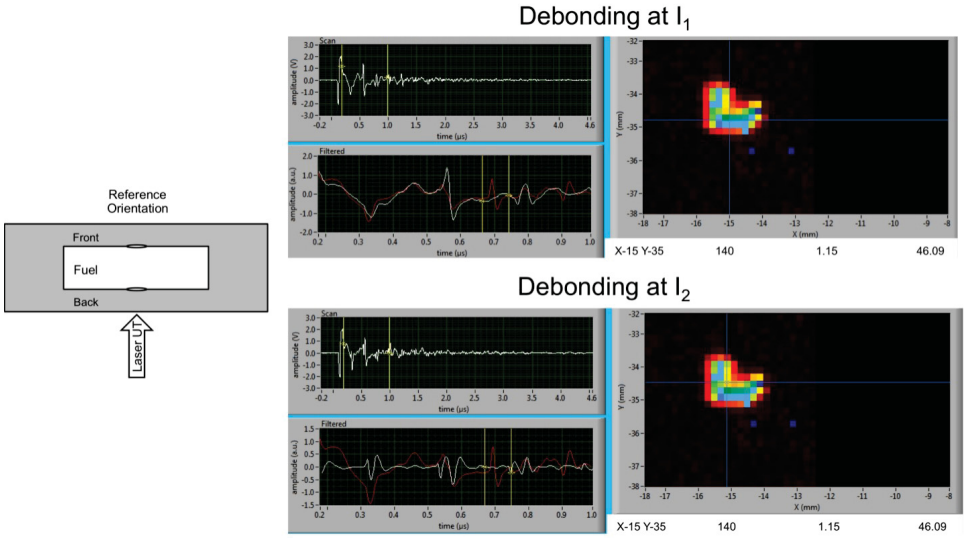

Figure 10. Example of shocked fuel plate containing debonds at both interfaces, I_1 and I_2, inspected in the Reference Orientation.

Finally, it's worth highlighting that the laser-UT inspection is capable of distinguishing so-called "kissing bonds", which can be considered to be an interface that is either not bonded but remains in intimate physical contact, or alternatively, which is significantly damaged after passage of a shock wave and remains only weakly bonded. Kissing bonds have been a subject of interest in the past as they are difficult to detect using conventional UT methods. An example of this type of behavior for a fuel plate containing a known debond at interface I1, that was inspected in the Reference Orientation, is shown in Figure 11. It's important to note the cursor position corresponding to the displayed white signal is located at the very edge of the apparent debond seen in the C-scan image. Careful examination of the white signal, compared to the well bonded signal (in red), shows that a reflection from interface I1, a reflection from the top (front) surface and a peak corresponding to the reverberation within the fuel are all present. This is only possible if some amount of wave energy is transmitted through the debond, indicative of a kissing bond at this location. The potential impact of kissing bonds on fuel performance is currently not known, and the LST method provides an opportunity to evaluate their impacts.

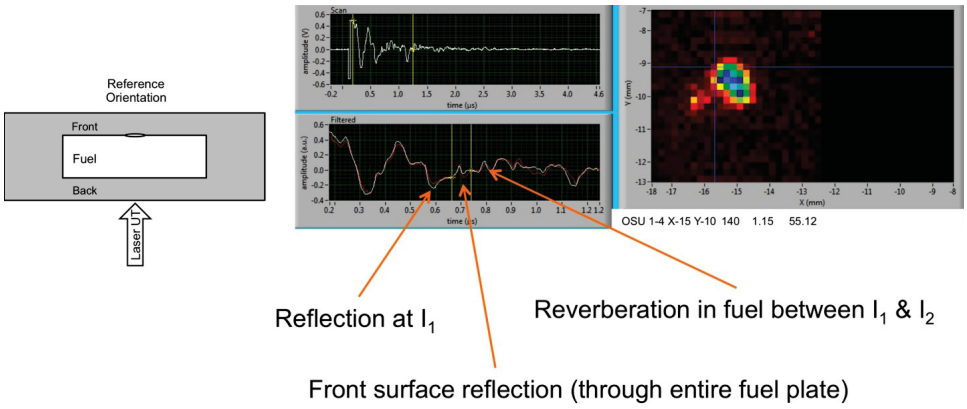

Figure 11. Example of shocked fuel plate containing a debond at interface I_1 inspected in the Reference Orientation, demonstrating the ability to detect a kissing bond near the edge of a known debond.

4.4 Laser-UT Dimensional Characterization

The experiments performed with the OSU-1-4 fuel plate were designed to elucidate the total measurement variations in the fuel plates, which consist of variations arising from the measurement system and from the variations within the specimens. The initial measurements were conducted using a constant flash lamp setting of 155 µs, using a fresh spot location for each test, and by considering a larger number of sample locations over nominally "identical" material.

The geometrical and material properties have been obtained by using the following experimental methodology. Measurements are taken at each shock location using laser ultrasonic A-scans before testing.

1. Measure total plate thickness (using calibrated micrometers)
2. Measure thickness of front cladding above the fuel
3. Measure thickness of back cladding below the fuel
4. Calculate thickness of fuel foil
5. Measure sonic velocity in the fuel.

The thicknesses of the front and back cladding (above and below the fuel, respectively) are calculated by noting the appropriate time of flight from each interface in the ultrasonic echo and knowing the (measured) speed of sound in the cladding. The fuel thickness is calculated by subtracting the sum of the front and back cladding thicknesses from the total plate thickness. The speed of sound in the fuel is measured by determining the time of flight (TOF) obtained from front and back surface reflections in the ultrasonic echo. The calculated fuel thickness and TOF are then used to calculate the ultrasonic velocity in the fuel. Speed of sound in a material can be related to the elastic modulus of a material by Equation 8. Thus the moduli for the aluminum cladding and foil can be monitored and used as inputs into fuel performance models as well as for interpreting post-irradiation examination results, e.g. swelling behavior.

Using these procedures, the thicknesses, average and standard deviation (STD), and fuel velocities were determined at several locations on the OSU-1-4 fuel plate sample. Results are listed in Table 2.

Table 2. OSU-1-4 thicknesses and fuel velocity determined from laser-UT characterization.

OSU 1-4 Location	Total thickness, mm	Front cladding thickness, mm	Back cladding thickness, mm	Fuel thickness, mm	Fuel velocity, mm/μs
X-10 Y-10	1.503	0.498	0.677	0.327	3.021
X-20 Y-25	1.508	0.473	0.694	0.341	3.112
X-10 Y-35	1.499	0.473	0.684	0.341	3.145
X-10 Y-05	1.503	0.460	0.684	0.359	3.203
X-15 Y-30	1.506	0.489	0.684	0.333	3.139
X-10 Y-25	1.505	0.477	0.723	0.306	2.985
Mean / STD	1.505 / 0.003	0.478 / 0.020	0.697 / 0.0178	0.330 / 0.021	3.079 / 0.103

In general, cladding thickness measurements rely on accurate measurement of the speed of sound in the cladding, which can vary according to the raw materials and processing used in fuel plate manufacturing. Time of flight measurements in cladding-cladding areas of a fuel plate allow for accurate velocity measurements and velocity mapping of individual plates. Unfortunately, velocity measurement for 6061 Al in the OSU-1-4 plate was not possible because the cladding-cladding regions were sheared off prior to receipt of the sample. Therefore, analysis of the OSU-1-4 data relied upon using an assumed 6061 Al sound velocity value that was the same as measured for the HIP 88 plates, 6.44 mm/μs (see below). As a check on the calculations, the sum of the calculated individual layer thicknesses was confirmed to agree with the total plate thickness measured independently using calibrated micrometers.

It's worth noting the relatively low standard deviations and therefore reasonable dimensional accuracy of these measurements. These results show the OSU-1-4 fuel plate is geometrically consistent, although the back cladding thickness and fuel thickness exhibit apparent variability at locations X-10 Y-10 and X-10 Y-25. Note that there is a significant difference between the front cladding thickness and back cladding thickness for this fuel plate, which indicates the fuel is not centered within the plate. There was no fabrication specification that addressed this feature and the impacts of this asymmetry on fuel performance are currently unknown. This is a subject of current investigation.

Similar measurements were carried out on the HIP 88 mini-plates and these results are listed in Table 3.

Table 3. HIP-88 plate geometries and fuel velocities determined from laser-UT characterization.

HIP-88 Plate ID	Total thickness, mm (Mean/STD)	Front cladding thickness, mm (Mean/STD)	Back cladding thickness, mm (Mean/STD)	Fuel thickness, mm (Mean/STD)	Fuel velocity, mm/μs (Mean/STD)
88-2	1.66 / 0.001	0.74 / 0.007	0.62 / 0.004	0.30 / 0.003	3.36 / 0.019
88-3	1.68 / 0.018	0.74 / 0.011	0.62 / 0.003	0.32 / 0.014	3.61 / 0.130
88-5	1.71 / 0.012	0.76 / 0.009	0.64 / 0.006	0.31 / 0.002	3.26 / 0.033

The measurements made on the HIP 88 plates demonstrate remarkable consistency for a laboratory scale fabrication process. The average sound velocity for 6061 Al in the HIP 88 plates is 6.44 mm/μs with a standard deviation of 0.024 mm/μs. Keep in mind that the "uncertainty" in the ultrasonic measurements is absorbed by the fuel thickness calculation, which is reflected in the correspondingly larger standard deviation values for fuel thickness in Tables 2 and 3.

Note there are significant differences in the measured fuel velocities. In particular, the data in Table 3 indicates that the LEU fuel (HIP 88-3) velocity is significantly higher than the other two fuels produced from DU. According to Equation 8, this likely indicates the Young's modulus of the LEU fuel is higher, although differences in density cannot be ruled out since density of the fuel was not independently measured in this work.

Variations in the fuel plate thickness with location within each plate were noted in the HIP 88 plates. To illustrate this, considering averages across all three plates, the plate thickness for the northwest and southwest corners were 1.71±0.01 and 1.71±0.02 mm, respectively, whereas plate thickness for the northeast and southeast corners were 1.61±0.10 and 1.58±0.04 mm, respectively. Since the plates were HIPed in a vertical position, the difference in plate thicknesses between the west and east sides of the plates probably originated from post-HIP sanding and machining operations, not from the HIP process itself. There was no obvious correlation between velocity and corner position in the plates or between plates; the random nature of the velocity data also suggests the thickness differences were likely created during the machining process.

4.5 Preliminary Bond Strength Evaluations

One of the advantages of LST relates to the relatively small test area, providing the ability to conduct many measurements on a single sample. Figure 12 shows fuel plate OSU-1-4, the sample being approximately 1.75 in. x 2 in. in size, that was removed from a larger fuel plate. Locations that were laser shock tested are indicated with a black marker, and are traceable using X-Y coordinates to a fiduciary mark scribed on the specimen before testing.

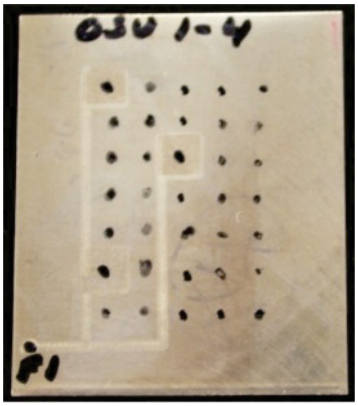

Figure 12. OSU-1-4 fuel plate sample after testing, showing fiduciary mark (lower left), multiple laser shock testing locations (black marker spots with ~ 0.25 in. spacing), and surface cleaning marks from laser-UT scanning (bright lines). Note, sample dimensions are approximately 1.75 in. x 2.0 in.

As discussed earlier, in effort to minimize the cumulative effects of plastic deformation, it is generally thought that the preferred methodology for conducting bond strength measurements involves using a fresh sample location for each laser shock shot, where the laser power is increased incrementally at each successive fresh specimen location until an interface debond is observed by laser-UT. However, since the effects of plasticity are not understood at this time, and because there's a desire to utilize the minimum specimen area possible, a second methodology was also investigated in this study, wherein the successive laser shots are applied to the same location, increasing the laser power at the same spot until a debond is observed. Results from these two methods of testing are presented below.

It was found to be most convenient for varying laser power in these experiments to adjust the flash lamp delay of the laser. This was accomplished by initially setting the flash lamp delay to 160 μs, and then decreased the value by 5 μs for each successive shot, continuing until a debond was detected by laser-UT in the post-shock scan.

Bond strength characterization results for the OSU-1-4 fuel plate sample are shown in Table 4, using the simplified analysis approach described in Section 4.1. The OSU-1-4 plate shock measurements used a flash lamp setting of 155 μs on fresh material with a larger number of sample locations over nominally "identical" material. The plate was also tested in the Flipped Orientation to assess if the significant fuel asymmetry affects the measured bond strength.

Although the data is preliminary and a larger population of test data is needed to draw definitive conclusions, a few trends are indicated Table 4. The shock velocity data suggest that debonding preferentially occurs at the interface I_1, which corresponds to the thin cladding side of the plate (Table 4). For the sample tested in the Reference Orientation, the debond threshold is suggested to occur for a maximum surface velocity between 30 and 35 m/s corresponding to a calculated bond strength between 525 and 650 MPa. For the same sample tested in the Flipped Orientation, the threshold appears to be closer to maximum surface velocity exceeding 40 m/s corresponding to a calculated bond strength greater than 700 MPa.

Table 4. Bond strength characterization results based on maximum bottom surface velocity, u_B, for the OSU-1-4 fuel plate sample.

Testing Location	Flash lamp delay (μs)	u_B for intact interfaces multiple shots using fresh locations (m/s)	u_B for interface I_1 debond, multiple shots using fresh locations (m/s)	Simplified stress calculation (MPa)
Reference Orientation				
X-10 Y-35	155		35.21	608
X-30 Y-35	155		34.3	593
X-30 Y-05	155		34.22	591
X-20 Y-15	155	30.39		525
X-20 Y-25	155		37.67	651
Flipped Orientation				
X25Y-20	150		42.64	737
X25Y-15	155	42.14		728

Bond strength characterization results for the HIP 88 fuel plates and the HIP 45-2 SS surrogate fuel plate are shown in Table 5. The most consistent and obvious trend in Table 5 is that interface I_2 debonded first in all cases. Although cladding thicknesses were much more uniform than in the OSU-1-4 plate, all debonding in the HIP 88 plates also occurred on the thin cladding side, consistent with the OSU-1-4 results. It appears that the highest bond strength of about 950 MPa was measured for HIP 88-2, which is the fuel plate that did not contain a Zr diffusion barrier layer. Should this result be confirmed, it's important to point that, although the pre-irradiation bond strength may be higher, presumably because of the formation of a (U-Mo)Al_x reaction layer, this layer is known to degrade in-reactor at intermediate burnup. Post-irradiation bond strength measurements might then be expected to reveal that samples without the Zr diffusion barrier layer exhibit weaker interfaces after irradiation.

The LEU fuel plate HIP 88-3 appears to have a slightly higher bond strength, approximately 800 MPa, compared to the HIP 88-5 plate produced using DU, which had a strength near 670 MPa, which is a value reasonably consistent with the results obtained on the OSU-1-4 plate having similar composition

and fabrication history. The HIP 45-1 plate, which had a SS surrogate fuel resulted in a bond strength similar to the DU plate containing a Zr diffusion barrier.

It's interesting to note that there does not appear to be a significant maximum surface velocity debond threshold difference between experiments conducted using the multiple shots using fresh spot method compared with the multiple shots at a single location method. This is a promising result suggesting that cumulative plasticity effects may not be significant, and the experimental method requiring less fuel plate area may be feasible. It does appear that the fresh location method requires more laser energy to achieve approximately the same maximum surface velocity debond threshold, which may be attributable to energy losses resulting from material yielding at each fresh spot location, whereas material is work hardened during the first shot when using the single spot method, resulting in less yielding on subsequent shots. At this time there is insufficient data to separate measurement system variations from materials variations and more samples will be tested in the future to investigate these effects.

Table 5. Bond strength characterization results based on maximum bottom surface velocity, u_B, for HIP mini-plates tested.

Plate ID	Flash lamp delay (μs)	u_B for interface I_2 debond, multiple shots at single location (m/s)	u_B for interface I_2 debond, multiple shots using fresh locations (m/s)	Simplified stress calculation (MPa)
88-2 DU no Zr	140	54.97		950
	135		55.79	964
88-3 LEU	150	40.85		706
	140		49.72	859
	140	47.22		816
88-5 DU Zr	150	36.34		628
	145		37.64	650
	150	42.23		731
45-2 SS	160	40.25		696
	155		36.35	628
	155		39.5	683

4.6 Advanced Bond Strength Calculations

Bond strength calculations were also performed by taking into account the multiple reflections involved in debonding an internal interface, as described in Section 3.1. The software program used to solve Equations 1 - 5 has a convenient user interface and reads the desired velocimeter output data file obtained from a shock experiment. It is up to the user to select the appropriate velocimeter output data file from a series of laser shock tests, based on the determination of the debond threshold and location of the debond, as described previously.

Based upon user input of the plate geometry (i.e. layer thicknesses), as well as density and speed of sound for each layer, the software uses the measured maximum surface velocity to calculate the stress as a function of time at each interface location, assuming either two terms or four terms, as described in Section 3.1. The software also displays the maximum stress value for each interface, which allows the user to compare the timing of the maximum stress at each interface to the velocimeter signal. As described in Section 4.4, the layer thicknesses and speed of sound in each layer may be measured during the experiments using the laser-UT system.

The following example from an experiment performed on the OSU-1-4 sample tested in the Reference Orientation at location X-10 Y-35 illustrates use of this software. This test was conducted using a flash lamp delay of 155 µs and found to exhibit a debond threshold at a maximum bottom surface velocity of 35.21 m/s. The velocimeter output, material and geometry inputs, and the results of the stress calculations using the model incorporating four terms are shown in Figure 13. It's possible to move the cursor position along the time axis and read the calculated stress value at each interface for the selected time, which allows a convenient comparison to be made between the peak interface stress and the maximum surface velocity in the velocimeter output signal.

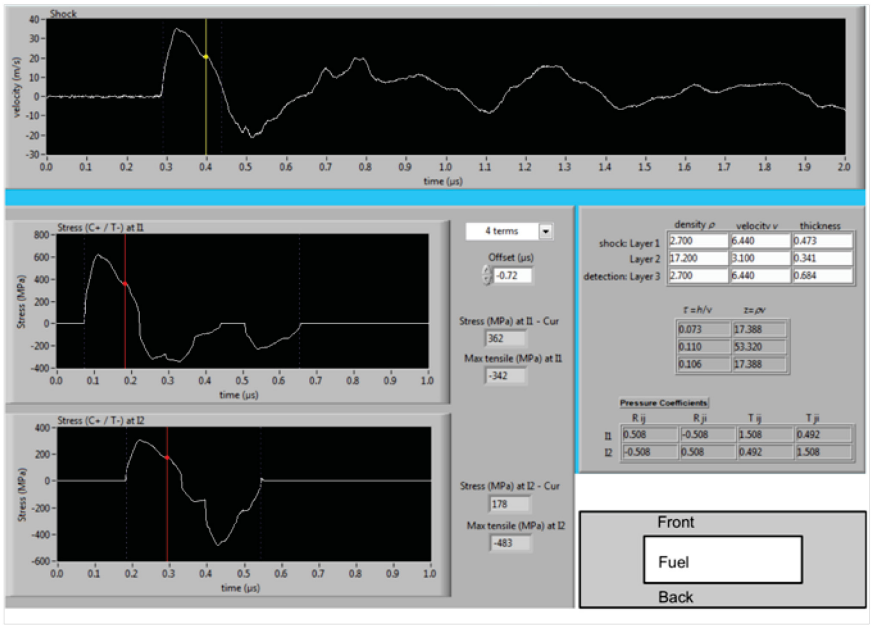

Figure 13. Example of bond strength calculation for the OSU-1-4 fuel plate sample after threshold testing in the Reference Orientation assuming four terms in the stress calculation.

The results of advanced bond strength calculations for the OSU-1-4 fuel plate test locations are shown in Table 6. This data shows that, in general, the advanced stress calculations predict smaller peak stresses at the interfaces than the stress calculated from the maximum bottom surface velocity alone. This is perhaps to be expected given that the velocimeter is detecting the arrival of the primary compression wave, which may be considered a measure of the energy that made it through the plate, and therefore an upper bound to the energy available to generate stresses at the internal interfaces later in time.

The advanced stress calculations for the OSU-1-4 geometry and materials properties predict that the bottom interface always exhibits a higher peak tensile stress, which is not in agreement with the observation for this sample tested in the Reference Orientation, where interface I_1, located near the top, always debonded first. The reason for this discrepancy is not clear at this time. It should be pointed out that when the OSU-1-4 sample was tested in the Flipped Orientation, interface I_1 is predicted to have the highest peak tensile stress, in agreement with the debond observations. As mentioned previously, the top cladding in this sample, adjacent interface I_1, was significantly thinner than the bottom cladding. In such cases, differences in residual stresses imposed on each of the interfaces, which will contribute to the total stress imposed on each interface during shock testing, may play a role. Fuel performance modeling of as-fabricated residual stresses for the case of significant cladding asymmetry is being explored to elucidate this behavior. However, it's worth noting that this observation is consistent with the behavior of irradiated fuel plates, which have been observed to exhibit debond failures consistently on the thin cladding side of the fuel plates. Another plausible explanation consistent with the observations is that interface I_1, for unknown reasons that related to processing history, may actually be weaker and therefore fails at a lower

peak stress value than interface I_2. Bulge testing and/or mini-cantilever beam testing, which may be able to isolate these interfaces, are planned at LANL on this fuel plate and may provide additional information. Finally, it's worth noting that, because of the significant asymmetry in the OSU-1-4 sample, the particular internal reflection terms included in the derivations of stress at the interfaces, based on the hypothetical fuel plate case shown in Figure 5 (see Appendix A), may not adequately represent the waves contributing to the peak tensile stress for this geometry. Additional elastic numerical simulations, similar to those used to generate Figure 5, need to be performed to address this question.

Note that, in general, the four term calculation predicts less difference in the peak stress values between the two interfaces compared to the two term calculation, and the peak stress for interface I_2 is little changed by the addition of the extra terms. It is expected that the top interfacial stress is more sensitive to the additional terms because the extra reflections originate from the interfaces toward the top of the specimen.

The results of advanced bond strength calculations for the HIP 88 fuel plates are shown in Table 7. Again, the advanced stress calculations predict smaller stresses at the interfaces than the stress estimated from the maximum bottom surface velocity. In this case, the calculations using two terms predict that the bottom interface will always exhibit higher peak tensile stress, which is consistent with the observation that interface I_2 always debonded first. Since all samples were tested in the Reference Orientation, which coincided with positioning the thinner cladding side adjacent the bottom surface, it's not possible from this data to determine if cladding asymmetry plays a role. For the calculations using four terms, the interface stresses are nearly equal, which may explain why there have been cases observed where both interfaces debond from a laser shot that exceeds the debond threshold (see e.g. Figure 10).

Table 6. Advanced bond strength calculation results for the OSU-1-4 sample.

Testing Location	Flash lamp delay (μs)	Simplified stress calculation (MPa)	Maximum tensile stress at interface, assuming two terms (MPa)		Maximum tensile stress at interface, assuming four terms (MPa)	
			I_1	I_2	I_1	I_2
Reference Orientation						
X-10 Y-35	155	608	225	463	349	481
X-30 Y-35	155	593	219	452	350	450
X-30 Y-05	155	591	217	453	324	424
X-20 Y-15*	155	525	196	398	275	396
X-20 Y-25	155	651	243	494	377	507
Flipped Orientation						
X25Y-20	150	737	559	275	559	543
X25Y-15*	155	728	552	272	552	549
* Indicates multiple laser shocks at one location.						

Table 7. Advanced bond strength calculation results for the HIP 88 min-plates.

Plate ID	Flash lamp delay (μs)	Simplified stress calculation (MPa)	Maximum tensile stress at interface, assuming two terms (MPa)		Maximum tensile stress at interface, assuming four terms (MPa)	
			I_1	I_2	I_1	I_2
88-2 DU no Zr	140*	950	341	734	712	701
	135	964	345	746	736	737
88-3 LEU[a]	150*	706	237	560	617	572
	140	859	296	675	700	691
	140*	816	280	642	674	639
88-5 DU Zr	150*	628	229	482	468	456
	145	650	237	499	502	535
	150*	731	264	562	556	552
45-2 SS	160*	696	271	516	317	655
	155	628	241	470	300	562
	155	683	268	504	302	651

[a] Assumed the same density value as DU.

* Indicates multiple laser shocks at one location.

Note that the stresses calculated for HIP 45-2 plate tested in the Reference Orientation using the two different models behave differently compared to the HIP 88 plates. In this case, a significantly lower peak tensile stress is calculated for the top interface (I_1) in the four-term calculations. HIP 45-2 debonded at interface I_2, consistent with the predictions. These calculation results demonstrate the sensitivity of the peak tensile stress values at each interface to relative differences in input material properties.

In summary, the advanced stress calculations presented here tend to predict that the bottom interface will have the highest peak tensile stresses. Thus one would generally expect that the bottom interface (I_2 for the case of Reference Orientation) would debond first during testing. However, testing of the OSU-1-4 plate has shown that debonding occurred 100% of the time at the interface with the thinnest cladding, regardless of orientation. Continued work to develop, validate and qualify the LST method will address the influences of cladding asymmetry, residual stresses, material properties, and variable interface strengths that have been discussed in this preliminary report.

5. SUMMARY

This report summarizes work conducted to-date on the implementation of new laser-based capabilities for characterization of bond strength in nuclear fuel plates, and presents preliminary results obtained from fresh fuel studies on as-fabricated monolithic fuel consisting of uranium-10 wt.% molybdenum alloys clad in 6061 aluminum by hot isostatic pressing. Characterization involves application of two complementary experimental methods, laser-shock testing and laser-ultrasonic imaging, collectively referred to as the Laser Shockwave Technique (LST), that allows the integrity, physical properties and interfacial bond strength in fuel plates to be evaluated. Example characterization results are provided, including measurement of layer thicknesses, elastic properties of the constituents, and the location and nature of generated debonds (including kissing bonds). LST provides spatially localized, non-contacting measurements with minimum specimen preparation, and is ideally suited for applications involving radioactive materials, including irradiated materials. The theoretical principles and experimental approaches employed in characterizing nuclear fuel plates are described, and preliminary bond strength measurement results are discussed, with emphasis on demonstrating the capabilities and limitations of these methods. These preliminary results demonstrate the ability to distinguish bond strength variations between different fuel plates. Although additional development work is necessary to validate and qualify the test methods, these results suggest LST is viable as a method to meet fuel qualification requirements to demonstrate acceptable bonding integrity.

6. REFERENCES

1. PLN-4291, "Project Execution Plan: U.S. High Performance Research Reactor Fuel Development Project," INL/INT-05-01009, Idaho National Laboratory, June 2013.
2. U.S. High Performance Research Reactor Project: Functions and Requirements, April, 2013.
3. J. L. Vossen, ASTMM Spec. Tech. Publ., **640**, pp. 122-131 (1978).
4. Gupta V, Argon A S, Cornie J A and Parks D M, Measurement of interface strength by laser-pulse-induced spallation *Mater. Sci. Eng.* A **126,** 1990, 105–17.
5. Yuan J and Gupta V 1993 Measurement of interface strength by the modified laser spallation technique: I. Experiment and simulation of the spallation process *J. Appl. Phys* .**74** 2388–97.
6. Gupta V and Yuan J 1993 Measurement of interface strength by the modified laser spallation technique: II. Applications to metal/ceramic interfaces *J. Appl. Phys.* **74** 2397–404.
7. Yuan J, Gupta V and Pronin A 1993 Measurement of interface strength by the modified laser spallation technique: III. Experimental optimization of the stress pulse *J. Appl. Phys.* **74** 2405–10.
8. C. Bolis, L. Berthe, M. Boustie, M. Arrigoni, S. Barradas, and M. Jeandin, Physical Approach to Adhesion Testing Using Laser- Driven Shock Waves, J. Phys. D: Appl. Phys., 2007, 40(10), p. 3155-3163.
9. M. Perton, A. Blouin and J.-P. Monchalin, "Adhesive bond testing of carbon–epoxy composites by laser shockwave," J. Phys. D: Appl. Phys., 44(3), 2011, 034012.
10. M. Arrigoni, S. Barradas, M. Braccini, M. Dupeux, M. Jeandin, M. Boustie, C. Bolis, L. Berthe, Comparative study of three adhesion tests (EN 582 similar to ASTM C633 - LASAT (LASer Adhesion Test) - Bulge and blister test) performed on plasma sprayed copper deposited on aluminum 2017 substrates, Journal of Adhesion Science Technology, 20 (5) pp. 471–487 (2006).
11. M. Perton, et al., "Laser shockwave technique for characterization of nuclear fuel plate interfaces", 39th Annual Review of Progress in QNDE, AIP Conf. Proc. 1511, 2013, 345-352.
12. M. Arrigoni, J.P. Monchalin, A. Blouin, S.E. Kruger, and M. Lord, Laser Doppler Interferometer Based on a Solid Fabry- Perot Etalon for Measurement of Surface Velocity in Shock Experiments, Meas. Sci. Technol., 2009, 20(1), p. 015302.
13. J. A. Smith; D. L. Cottle and B. H. Rabin, "Laser Shockwave For Characterizing Diffusion Bonded Interfaces, to be published in AIP Conf. Proc. Vol. 151, D. O. Thompson, D. E. Chimenti, Editors, American Institute of Physics, Melville, NY, 2014.
14. J. A. Smith et al., "Laser Shockwave Technique For Characterization Of Nuclear Fuel Plate Interfaces," RERTR 2012 — 34th International Meeting On Reduced Enrichment For Research And Test Reactors, Warsaw Marriott Hotel Warsaw, Poland, October 14-17, 2012.
15. Jue, J. F., Park, B. H., Clark, C. R., Moore, G. A., Keiser, D. D., "Fabrication of Monolithic RERTR Fuels by Hot Isostatic Pressing," *Nuclear Technology,* 172.2 (2009), pp. 204-210.
16. G. A. Moore and M. C. Marshall, "Co-Rolled U10Mo/Zirconium-Barrier-Layer Monolithic Fuel Foil Fabrication Process," INL/EXT-10-17774, Idaho National Laboratory, January 2010.
17. B. H. Park, C. R. Clark and J. F. Jue, "INL HIP Plate Fabrication," INL/EXT-10-17792, Idaho National Laboratory, February 2010.
18. Jue, J. F., private communication.

19. “Fabrication Control Plan for Test Plates Intended for Oregon State University Hydro-Mechanical Fuel Testing Facility,” PLN-3838, Idaho National Laboratory, May 2011.
20. “Specification for HMFTF Test Plates,” SPC-1316, Idaho National Laboratory, December 2010.
21. L. Davison, D. E. Grady, M. Shahinpoor, *High-Pressure Shock Compression of Solids II*, Springer-Verlag, New York, 1996.
22. J. R. Asay, M. Shahinpoor, *High-Pressure Shock Compression of Solids*, Springer-Verlag, New York, 1993.
23. R. A. Graham, Solids Under High-Pressure Shock Compression, Springer-Verlag, New York, 1993.

Appendix A

Derivation of Stress Equations

INTENTIONALLY BLANK

Appendix A

Derivation of Stress Equations

The ability to estimate internal stress from the measured bottom surface velocity is based on the fundamental relationship from acoustics between stress s and particle velocity u:

$$\sigma = \pm z u \qquad z_i (u_{inc} - u_{ref}) = z_j u_{trm} \tag{A1}$$

where is the acoustic impendence (ρ is density, v is wave velocity), the ± sign relates to the direction of wave propagation arriving at the interface, the indices *inc*, *ref* and *trm* are, respectively, for incident, reflected and transmitted waves and *i,j* refer to the layers, respectively for the incident and transmitted waves. The stress value is positive for a compressive wave and negative for a tensile wave. One has the reflection and transmission coefficients for the particle velocity (or displacement) amplitude as:

$$R_{ij}^u = \frac{z_i - z_j}{z_i + z_j} \qquad T_{ij}^u = \frac{2z_i}{z_i + z_j} \tag{A2}$$

while for pressure amplitude:

$$R_{ij}^p = \frac{z_j - z_i}{z_i + z_j} = -R_{ij}^u \qquad T_{ij}^p = \frac{2z_j}{z_i + z_j} = \frac{z_j}{z_i} T_{ij}^u \tag{A3}$$

Also the travel time of the wave in a given layer *i* of thickness *h* is $\tau_i = h_i / v_i$.

The stress at the interface I_1 at the time of rupture t_{r1} is calculated from the particle velocities of the 4 waves present at that time and that position (see Figure 5):

$$\sigma_1 = z_2 u_{01} - z_1 u_{0121} + z_2 u_{0101} - z_1 u_{012321} \tag{A4}$$

where u_{01}, u_{0121}, u_{0101} and u_{012321} refer to the waves that propagated from the top surface to the interface I_1, after successive reflections and transmissions denoted 0, 1, 2, 3, respectively for the top surface, the interfaces I_1, I_2 and the bottom surface. Each component, as well as the velocimeter signal at the bottom surface, $u(t) = u_{0123}$, can be expressed using the particle velocity of the wave generated at the top surface u_0(t) at time t=0. The different wave components are:

$$\begin{aligned}
u_{01}(t) &= u_0(t - \tau_1) T_{12}^u \\
u_{0121}(t) &= u_0(t - \tau_1 - 2\tau_2) T_{12}^u R_{23}^u T_{21}^u \\
u_{0101}(t) &= u_0(t - \tau_1 - 2\tau_1) R_{12}^u (+1) T_{12}^u \\
u_{012321}(t) &= u_0(t - \tau_1 - 2\tau_2 - 2\tau_3) T_{12}^u T_{23}^u (+1) T_{32}^u T_{21}^u \\
u_{0123}(t) &= u_0(t - \tau_1 - \tau_2 - \tau_3) T_{12}^u T_{23}^u (2) = u(t)
\end{aligned} \tag{A5}$$

It is noticed that the wave component u_{0123} can be identified to the bottom surface velocity $u(t)$ only for time $t < t_{min1}$ in Figure 5. Successive changes of variables from t to t' allow resynchronization at the interface while obtaining the direct relation between each component and the velocimeter signal as:

$$
\begin{aligned}
u_{01}(t') &= u(t' + \tau_2 + \tau_3)/2T_{23}^u \\
u_{0121}(t') &= u(t' - \tau_2 + \tau_3)R_{23}^u T_{21}^u / 2T_{23}^u \\
u_{0101}(t') &= u(t' - 2\tau_1 + \tau_2 + \tau_3)R_{12}^u / 2T_{23}^u \\
u_{012321}(t') &= u(t' - \tau_2 - \tau_3)T_{23}^u T_{32}^u T_{21}^u / 2T_{23}^u
\end{aligned}
\tag{A6}
$$

Using Eq. (A4), the stress at the first interface at time t_{r1} then becomes:

$$
\sigma_1(t_{r1}) = \frac{z_2}{2T_{23}^u}\begin{pmatrix} u(t_{r1} + \tau_2 + \tau_3) - R_{23}^u T_{21}^u \dfrac{z_1}{z_2} u(t_{r1} - \tau_2 + \tau_3) + R_{12}^u u(t_{r1} - 2\tau_1 + \tau_2 + \tau_3) \\ - T_{23}^u T_{32}^u T_{21}^u \dfrac{z_1}{z_2} u(t_{r1} - \tau_2 - \tau_3) \end{pmatrix}
\tag{A7}
$$

Alternatively, substitution of the reflection and transmission coefficients in pressure amplitude leads to the final expression for stress with 4 terms:

$$
\sigma_1(t_{r1}) = \frac{z_3}{2T_{23}^P}\begin{pmatrix} u(t_{r1} + \tau_2 + \tau_3) + R_{23}^p T_{21}^p u(t_{r1} - \tau_2 + \tau_3) - R_{12}^p u(t_{r1} - 2\tau_1 + \tau_2 + \tau_3) \\ - T_{23}^p T_{32}^p T_{21}^p u(t_{r1} - \tau_2 - \tau_3) \end{pmatrix}
\tag{A8}
$$

If one considers only back propagation and forward propagation excluding internal reflections, one has Eq. (A8) only with the first and fourth terms.

The stress at the interface I_2 at time t_{r2} is calculated in the same way. Assuming no debond at the first interface, one has (see Figure 5):

$$
\sigma_2 = z_3 u_{012} - z_2 u_{01232} + z_3 u_{01012} + z_3 u_{01212}
\tag{A9}
$$

where u_{012}, u_{01232}, u_{01012} and u_{01212} refer to the waves that propagated from the top surface to the interface I_2, after successive reflections and transmissions. Each component, as well as the velocimeter signal at the bottom surface, can be expressed using the particle velocity of the wave generated at the top surface u_0(t). The different wave components are:

$$
\begin{aligned}
u_{012}(t) &= u_0(t - \tau_1 - \tau_2)T_{12}^u T_{23}^u \\
u_{01232}(t) &= u_0(t - \tau_1 - \tau_2 - 2\tau_3)T_{12}^u T_{23}^u (+1) T_{32}^u \\
u_{01012}(t) &= u_0(t - 3\tau_1 - \tau_2)R_{12}^u (+1) T_{12}^u T_{23}^u \\
u_{01212}(t) &= u_0(t - \tau_1 - 3\tau_2)T_{12}^u R_{23}^u R_{21}^u T_{23}^u \\
u_{0123}(t) &= u_0(t - \tau_1 - \tau_2 - \tau_3)T_{12}^u T_{23}^u (2) = u(t)
\end{aligned}
\tag{A10}
$$

Again, the wave component u_{0123} can be identified to the bottom surface velocity $u(t)$ only for time $t < t_{min1}$ in Figure 5. Successive changes of variables from t to t' allow resynchronization at the interface while obtaining the direct relation between each component and the velocimeter signal as:

$$
\begin{aligned}
u_{012}(t') &= u(t'+\tau_3)/2 \\
u_{01232}(t') &= u(t'-\tau_3)T_{32}^{u}/2 \\
u_{01012}(t') &= u(t'-2\tau_1+\tau_3)R_{12}^{u}/2 \\
u_{01212}(t') &= u(t'-2\tau_2+\tau_3)R_{23}^{u}R_{21}^{u}/2
\end{aligned}
\tag{A11}
$$

Using Eq. (A9), the stress at the second interface at time t_{r2} then becomes:

$$
\sigma_2(t_{r2}) = \frac{z_3}{2}\begin{pmatrix} u(t_{r2}+\tau_3) - T_{32}^{u}\dfrac{z_2}{z_3}u(t_{r2}-\tau_3) + R_{12}^{u}u(t_{r2}-2\tau_1+\tau_3) \\ + R_{23}^{u}R_{21}^{u}u(t_{r2}-2\tau_2+\tau_3) \end{pmatrix}
\tag{A12}
$$

Alternatively, substitution of the reflection and transmission coefficients in pressure amplitude leads to the final expression for stress with 4 terms:

$$
\sigma_2(t_{r2}) = \frac{z_3}{2}\begin{pmatrix} u(t_{r2}+\tau_3) - T_{32}^{p}u(t_{r2}-\tau_3) - R_{12}^{p}u(t_{r2}-2\tau_1+\tau_3) \\ + R_{23}^{p}R_{21}^{p}u(t_{r2}-2\tau_2+\tau_3) \end{pmatrix}
\tag{A13}
$$

If one considers only back propagation and forward propagation excluding internal reflections, one has Eq. (A13) only with the first and second terms.